Acta Materialia 227 (2022) 117686

Contents lists available at ScienceDirect

Acta Materialia

journal homepage: www.elsevier.com/locate/actamat

Full length article

Design of high strength and wear-resistance β-Ti alloy via oxygen-charging

Xiu-Qun Wang[a], Yu-Sheng Zhang[b], Wei-Zhong Han[a,*]

[a] Center for Advancing Materials Performance from the Nanoscale, State Key Laboratory for Mechanical Behavior of Materials, Xi'an Jiaotong University, Xi'an 710049, China
[b] Xi'an Rare Metal Materials Institute Co. Ltd, 710016 Xi'an, China

ARTICLE INFO

Article history:
Received 31 October 2021
Revised 6 January 2022
Accepted 23 January 2022
Available online 24 January 2022

Keywords:
β-Ti
Oxygen-charging
Hardening
Wear
Toughness

ABSTRACT

Titanium (Ti) is a promising biomedical material due to its superior corrosion resistance, low elastic modulus and favorable biocompatibility. Nevertheless, Ti faces a dilemma because of its inferior abrasion performance and strength-ductility trade-off, which poses a limitation in application as biomedical implants. Here, we developed an oxygen-charging method to fabricate a β-Ti alloy with combination of ultrahigh surface hardness, strength, toughness and remarkable wear resistance. The superior mechanical performance of β-Ti alloy originates from a 200 μm-thick α+β phase hard shell, a 600 μm oxygen gradient region and an oxygen-free β-Ti core. The gradient phase and composition structures display different deformation mechanisms, transforming from simple but unusual basal slip in α phase to multiple-slip activities in β phase. The unique oxygen gradient distribution makes β-Ti alloy much stronger and tougher that can resist surface crack propagation and sample catastrophic failure. Oxygen charging is a novel technique to design high-performance Ti implants for biomedical applications.

1. Introduction

Titanium (Ti) alloys are indispensable engineering structural and functional materials for application in aerospace [1,2] and biomedical [3,4] fields due to its lightweight, high strength-to-weight ratio, excellent corrosion resistance [5,6] etc. Ti has two allotropic phases, a hexagonal-close-packed (HCP) α phase below 882 °C and a body-centered-cubic (BCC) β phase above [7]. With the addition of β-stabilizers (such as Mo, Nb, Cr) and appropriate heat treatment, the metastable β phase forms at room temperature [7]. Due to lower elastic modulus, enhanced biocompatibility and superior corrosion resistance [8], β-Ti alloys are regarded as promising human permanent implants [9]. Nevertheless, accidents of loosening or even failure of orthopedic implants caused by joint friction [10,11] pose a challenge in design and manufacture of biomedical β-Ti alloys. Several surface modifications [12–15] were proposed to improve hardness and surface abrasion performance of Ti implants. However, potential hazards of coating failure and high cost make surface modification an unfavorable choice.

Recently, thick oxide layer of metals as an antibiotics coating [16] exhibits high abrasive resistance [17], which inspires researchers to employ oxygen to tune the performance of biomedical materials. Oxygen diffusion hardening was proposed to process Ti alloy, while the obtained alloys have a thick but loose oxide layer and an inferior mechanical performance [18–20]. Acting as α stabilizer, oxygen has tremendous impact on Ti phase stability [21] and mechanical properties [22,23]. Ti has high oxygen solid solubility of 14.5 wt.% in α phase and 2 wt.% in β phase [24]. A small amount of oxygen solutes in Ti leads to marked strengthening but unfortunately considerable reduction in ductility [25]. Such alloying induced strength-ductility tradeoff is a common phenomenon in many metals and alloys [26]. One approach to achieve strength-ductility synergy in biomaterials is design of gradient materials including gradient microstructures or compositions [27,28]. Gradient materials, such as gradient in grain size, twin thickness, bi-metal interface density etc., possess combination of high strength and excellent ductility, which is an effective mean to overcome strength-ductility trade-off [29–33]. Besides, compositional gradient materials also optimize mechanical properties and deformation behavior. Carburization or nitriding makes steels with superior surface hardening and enhanced wear resistance [34], but these surface treatments are mainly used for steels. Likewise, dilution of oxygen solutes also leads to an intense hardening effect [35]. Recently, a novel oxygen-charging method is proposed to tune the mechanical properties and corrosion behavior of BCC metals [36–39]. For example, a quadruple yield strength of Nb without sacrifice of uniform ductility has been achieved by formation of oxygen gradient [36]. Notably, the oxygen charging is also suitable for metals and

* Corresponding author.
E-mail address: wzhanxjtu@mail.xjtu.edu.cn (W.-Z. Han).

https://doi.org/10.1016/j.actamat.2022.117686
1359-6454/

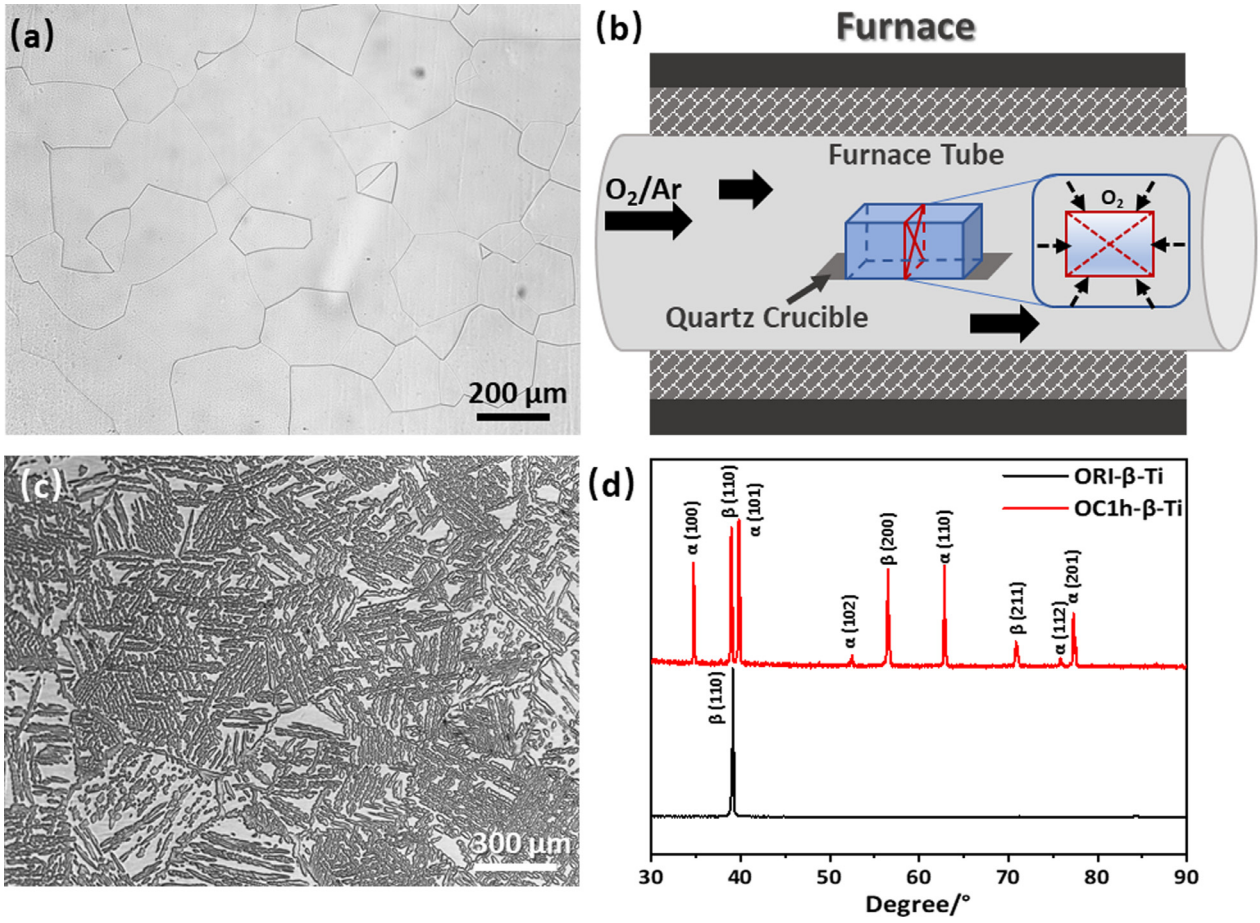

Fig. 1. (a) Microstructures of ORI-β-Ti. (b) Cartoon of the oxygen-charging experimental setup for fabrication of oxygen-gradient β-Ti. (c) Surface microstructures of oxygen-charged 1 h β-Ti. (d) XRD patterns of β-Ti before and after oxygen charging.

alloys with high temperature BCC phase. Therefore, design of oxygen solute gradient Ti component provides a brand new insight to develop high-performance biomedical materials.

In this study, we use an oxygen-charging technique to process a β-Ti alloy. The oxygen-charged sample has a 200 μm-thick $\alpha+\beta$ phase hard shell, a 600 μm oxygen gradient region and an oxygen-free β-Ti core. This β-Ti alloy with such novel gradient microstructures possesses ultrahigh hardness, strength, toughness and marked abrasive resistance. Besides, such a β-Ti alloy resists surface crack propagation and catastrophic failure due to gradient microstructures and an oxygen-free ductile core. The oxygen-charging technique is a feasible and economical mean to achieve high-performance Ti implantation.

2. Materials and methods

2.1. Oxygen-charging processes

A metastable β-Ti alloy with nominal composition of Ti–5Al-4Mo-4V-4Cr-3Zr (wt.%) was used as model material. With addition of biocompatible β-stabilizers Mo, Cr, Zr and low amounts of baleful elements, such β-Ti alloy excels over widely-used Ti-6Al-4 V alloy for biomedical application. The β-Ti alloy ingots were solution-treated in β transus area followed by water quenching to obtain single β phase. The sample has an average grain size of 300 μm, as shown in Fig. 1(a). The solution-treated sample is named as ORI-β-Ti. Oxygen-charging treatment has four steps. First, putting the ORI-β-Ti sample in a tube furnace filled with a flowing mixture gas of oxygen and argon, as illustrated in Fig. 1(b). Second, heating the furnace to 1000 °C (in the β phase region). Third, keeping the sample for different time (1 h, 2 h, 4 h). Finally, the sample is water quenched to room temperature. The samples with 1 h, 2 h and 4 h of oxygen-charging are named as OC1h-β-Ti, OC2h-β-Ti and OC4h-β-Ti, respectively. During the oxygen-charging, the pressure inside the furnace tube was set to 400 Pa. The concentrations of oxygen, nitrogen, carbon at the surface of samples were measured by LECO ONH836 Oxygen/Nitrogen/Hydrogen Elemental Analyzer and LECO CS844 Carbon/Sulfur Analyzer, as listed in Table 1. After oxygen-charging, the concentration of oxygen increased significantly.

Table 1
Surface composition (wt.%) of carbon, nitrogen and oxygen in ORI-β-Ti specimens after oxygen charging for different time.

Sample/Content(wt.%)	Carbon	Nitrogen	Oxygen
ORI-β-Ti	0.0066	0.0076	*0.049*
OC1h-β-Ti	0.0150	0.0180	*0.887*
OC2h-β-Ti	0.0130	0.0140	*1.640*
OC4h-β-Ti	0.0092	0.0226	*3.400*

2.2. Microstructure characterization

The samples were electrolytically polished before microstructural examination. X-ray diffraction (XRD) with a Cu-Kα radiation was used to identify phase structures. HITACHI SU6600 scanning electron microscope (SEM) was applied for microstructural characterization. The compositions of the sample were analyzed using Energy Dispersive Spectrometer inside SEM. Phase structures and orientation relationship were determined using electron backscattered diffraction (EBSD). A high-resolution transmission electron

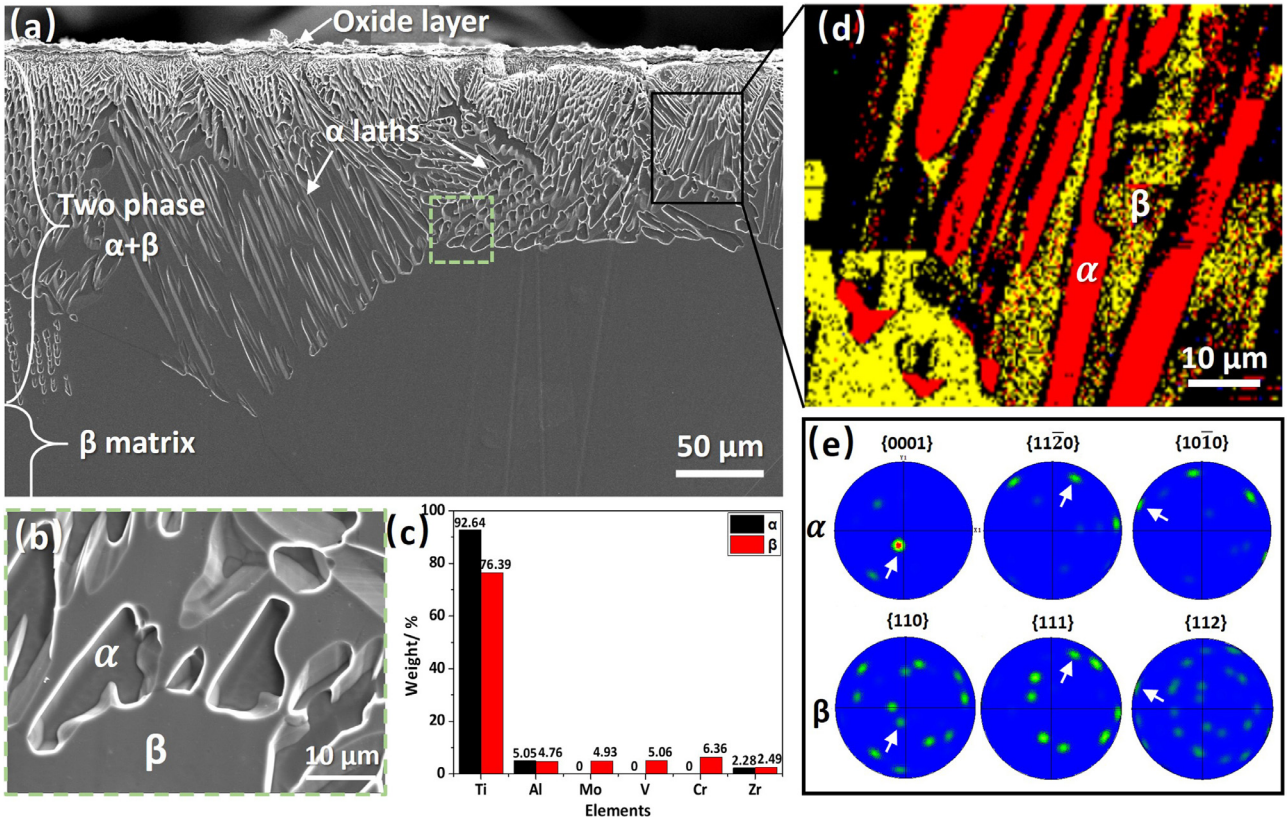

Fig. 2. (a) Cross-sectional SEM image of OC-β-Ti. (b) Enlarged image showing the region marked with green box in (a) that α phases form in β matrix. (c) Concentration of alloying elements in region (b). (d) Phase map of the region marked with black box in (a). (e) The orientation relationship between α and β phase can be determined according to the pole figures. (For interpretation of the references to colour in this figure legend, the reader is referred to the web version of this article.)

microscope (TEM) (JEOL 2100F) operating at 200 KV was utilized for deformation structures characterization. TEM foils were lift out by focused ion beam (FIB) from some of the indentations in the cross-section of an OC4h-β-Ti.

2.3. Mechanical tests

Vickers hardness were measured on the cross-section of oxygen-charged samples from one edge to the other with an applied load of 200 gf and a holding time of 10 s. Five repeated tests were performed for each site to ensure reproducibility. Bulk compression tests were conducted using column samples with size of 4 mm (diameter) × 7 mm (length) at a strain rate of 10^{-4} s^{-1}. More than three tests were repeated for each type of sample. Abrasion tests were conducted on a disk wear-testing machine with a rotation speed of 60 r•min^{-1}. The samples with a size of ϕ 5 mm × 8 mm were placed on the disk with applied load of 3 N. SiC sand papers (800#) were used as the abrasive substrate and placed between the tested samples and the disk. In abrasion tests, the sample was slid from center to rim of the disk with a constant speed of 4 mm•r^{-1}. The average weight loss from three repeating tests was used as the abrasive indicator. The wear weight loss per unit area was regarded as the wear rate. The abrasive wear behavior and the surface roughness after the wear tests were analyzed by 3D laser scanning microscope ((VK-9710, Osaka, Japan)).

3. Results

3.1. Phase structures in oxygen-charged β-Ti

The ORI-β-Ti has equiaxed grains with an average size of ~300 μm, as displayed in Fig. 1(a). Fig. 1(b) shows the cartoon of the oxygen-charging setup. The oxygen-charging method introduces not only a thin oxide layer on the top of the sample but also a wide region with oxygen gradient distribution [40]. Gaseous O_2 is converted into oxygen atoms/ions on the surface of Ti under high temperature. Oxygen atoms then continuously diffuse into the interior of the ORI-β-Ti [41]. After oxygen-charging, some lath phases are formed on the top surface of oxygen-charged β-Ti, as shown in Fig. 1(c). XRD patterns in Fig. 1(d) indicate that these lath phases are HCP α-Ti. The surface oxide layer has been removed by mechanical grinding before imaging and no oxide remained according to the XRD patterns in Fig. 1(d). Oxygen is known as α stabilizer, which promotes the formation of α-Ti [21]. In addition, oxygen also decreases the stability of inherently metastable BCC β-Ti, which leads to spinodal decomposition of β phase [42]. Once the oxygen concentration reaches a critical level, lath-shaped α-Ti starts to precipitate and permeate into β-Ti, thus α-Ti shell is formed on the surface of β-Ti after oxygen-charging.

Fig. 2(a) shows the cross-sectional microstructures of OC4h-β-Ti. Three distinct regions can be identified: a 10 μm oxide layer, a 200 μm α+β two phases region, and an equiaxed β-Ti matrix. The lath-shaped α phase with different shapes and orientations show a strong grain-dependence. The growth of α-Ti is limited within the grains [43], as shown in Fig. 2(a). Figs. 2(b) and (c) show the portioning of alloy elements in α and β phases. β stabilizers (Mo, V, Cr) are absent in the solute oxygen-induced α phase. Fig. 2(d) shows phase map of the region marked by black box in Fig. 2(a). The lath-shaped α phase has a classical Burgers orientation relationship with the β matrix, such as $\{0001\}_\alpha$// $\{110\}_\beta$, $\{11\bar{2}0\}_\alpha$// $\{111\}_\beta$, $\{10\bar{1}0\}_\alpha$// $\{112\}_\beta$, according to the pole figures in Fig. 2(e) [44].

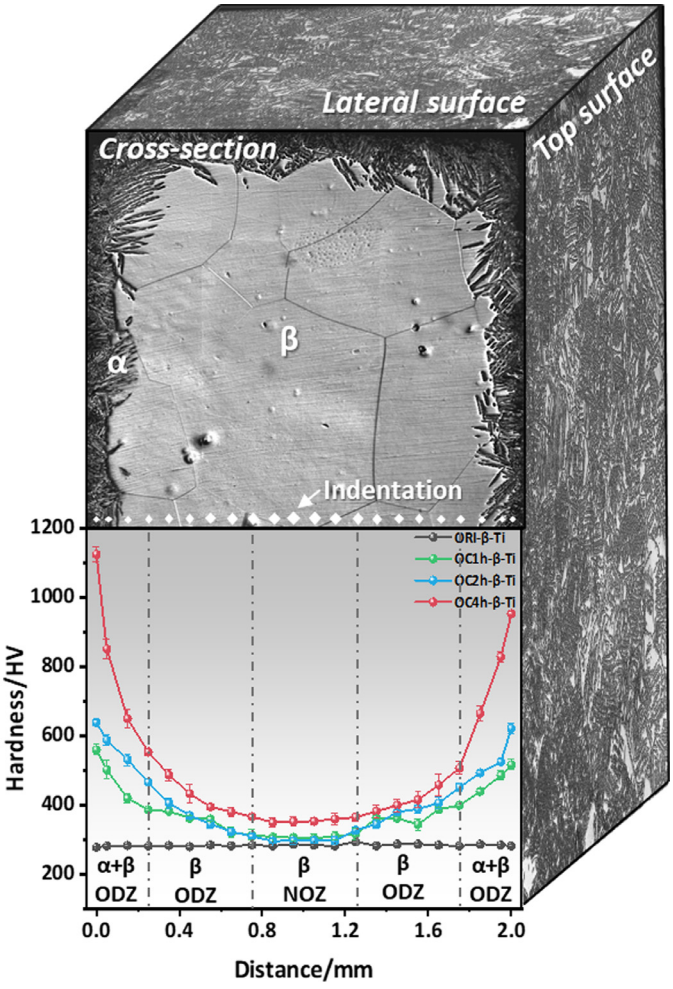

Fig. 3. Three-dimensional microstructures and hardness distribution of oxygen-charged β-Ti. HV is the unit for the Vickers hardness. Distribution of hardness in β-Ti after oxygen charging for different time is shown in lower part of the figure. The variation of hardness is related to different microstructures, such as $\alpha+\beta$ oxygen-dissolved zone (referred to as $\alpha+\beta$ ODZ), β oxygen-dissolved zone (referred to as β-ODZ) and β non-oxygen zone (referred to as β-NOZ).

3.2. Ultrahigh hardening in oxygen-charged β-Ti

Fig. 3 demonstrates three-dimensional microstructures of OC-β-Ti and the corresponding Vickers hardness distribution. The oxygen concentration decreases gradually from the sample's surface to interior. Similarly, the Vickers hardness also decreases from the top surface to the center of the sample, as shown in Fig. 3. The distribution of hardness reflects the gradient distribution of oxygen in the cross-section of oxygen-charged β-Ti. The subsurface hardness of the OC4h-β-Ti reaches 1125 HV, which is nearly quadrupled compared to that of ORI-β-Ti (284 HV). The subsurface hardness of OC4h-β-Ti is much higher than the maximum hardness that can be achieved by other surface modifications, such as ion implantation, electrochemical or thermal oxidation etc. [45–47]. The oxygen-charged β-Ti has a gradient microstructures and hardness distribution. A 200 μm thick $\alpha+\beta$ phases layer as a hard shell covers the β-Ti. The diffusion of solute oxygen reaches ~0.8 mm on each side of the samples after oxygen-charging. The surface oxygen concentration in the OC4h-β-Ti is about 3.4 wt.%, surging near 70 times of the oxygen concentration in the ORI-β-Ti, while the content of carbon and nitrogen maintains at the similar level.

By tuning the oxygen-charging time, i.e. kept for 1 h, 2 h, 4 h, distinction hardness gradient can be obtained, as displayed in Fig. 3. The hardness gradient becomes steeper with the elongation of oxygen-charging duration. The maximum hardness of oxygen-charged for 1 h, 2 h and 4 h reaches 560 HV, 640 HV and 1125 HV, respectively. According to the combination of microstructure heterogeneity and oxygen gradient, the cross-section of OC-β-Ti can be divided into three regions: a hard $\alpha+\beta$ two phases oxygen-dissolved zone (named as $\alpha+\beta$ ODZ), a β oxygen-dissolved zone (named as β-ODZ) and a ductile β non-oxygen zone (named as β-NOZ). Note that with the increasement of oxygen-charging time, the diffusing distance of oxygen solutes increases simultaneously. Therefore, the oxygen solutes diffuse throughout the whole sample in OC4h-β-Ti (Fig. 3).

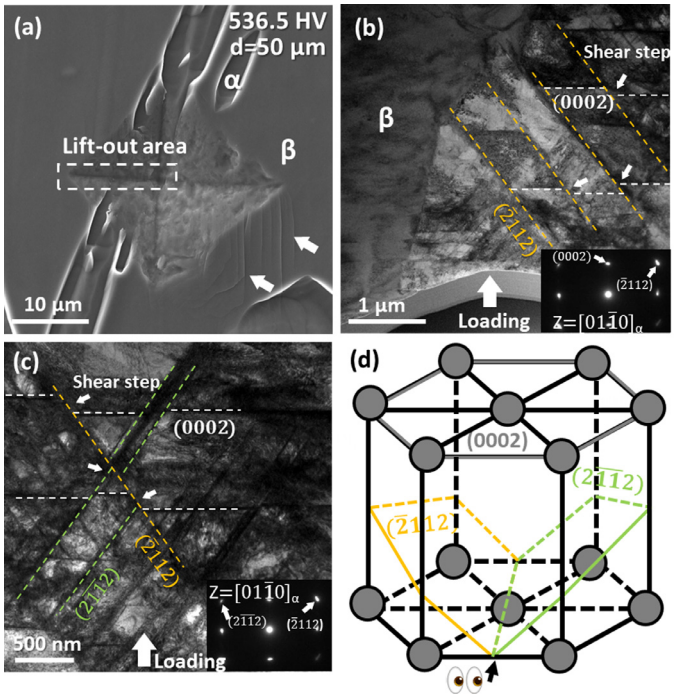

Fig. 4. Deformation mechanism in $\alpha+\beta$ ODZ. (a) SEM micrograph of an indentation in $\alpha+\beta$ ODZ. Hardness is marked in the right corner of the figure, d is the distance from the sample surface to the indentation site. (b) Typical TEM micrographs showing the characteristics of slip bands in α phase. (c) Intersection of slip traces in α phase under indentation. (d) Schematic showing the activation of slip planes in a hexagonal close-packed unit cell.

3.3. Oxygen-concentration dependent deformation mechanisms

Thin TEM foils were cut under some typical indentations to reveal the oxygen-gradient-controlled deformation mechanisms. Fig. 4(a) shows the SEM image of an indentation in the $\alpha+\beta$ ODZ, which is 50 μm from the top surface. Some wrinkles are formed at the right lower corner of the indentation in the β matrix region, as marked by arrows in Fig. 4(a). No slip trace was observed in the adjacent α lath, which means the α-laths are hard to deform. A thin TEM foil was cut at the location marked by the white dash line, where both α and β phases were included. Fig. 4(b) displays the deformation features just underneath the indentation. The brighter region with some straight slip bands is α-Ti, while the darker region is β matrix in which a homogeneous deformation characteristic can be identified. Fig. 4(b) shows the intersection of slip bands in α-phase along (0002) and ($\bar{2}$112). It is clear that the (0002) slip bands were cut by slip bands along ($\bar{2}$112), which means the slip along (0002) was initiated first. Fig. 4(c) shows a region slightly far away from the indentation region. Slip bands along (0002), ($\bar{2}$112) and (2$\bar{1}\bar{1}$2) planes were identified. Similarly, slip bands along basal plane (0002) were further sheared by ($\bar{2}$112)

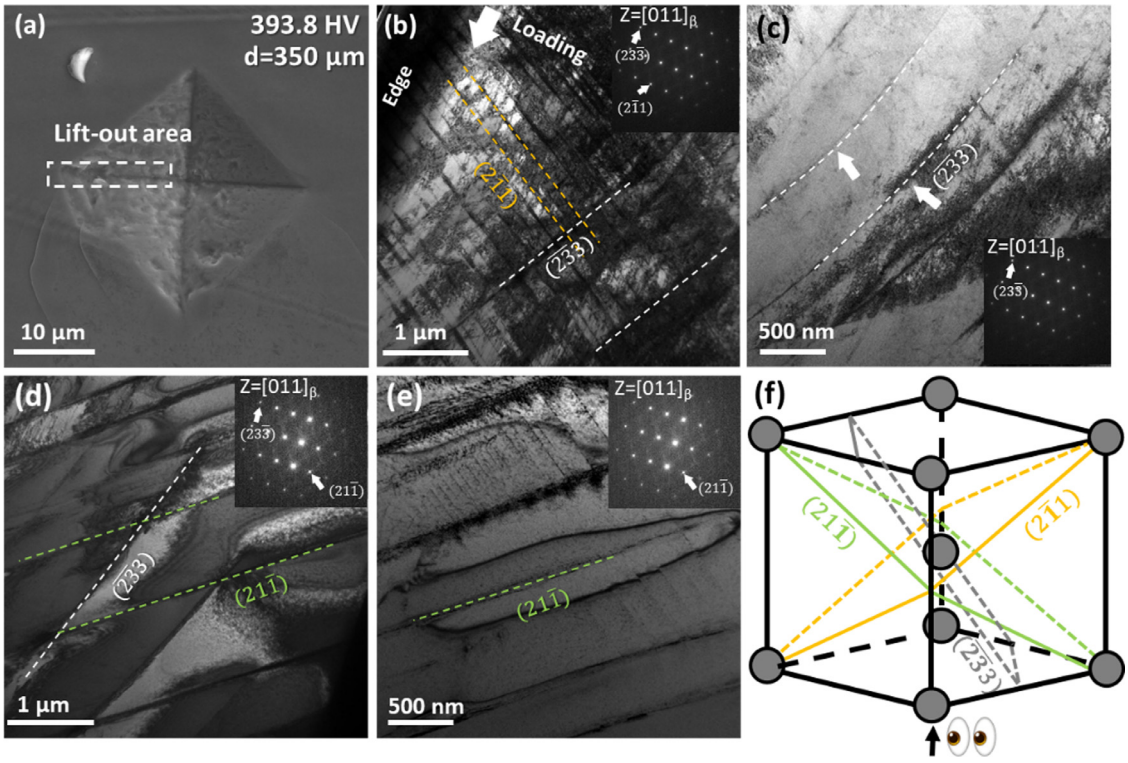

Fig. 5. Deformation mechanism in β-ODZ. (a) SEM micrograph of an indentation in β-ODZ. (b) TEM micrographs showing the parallel slip lines underneath indentation. (c) TEM image showing some curved slip trace along {233} plane. (d) Slip features underneath the edge of the indentation. (e) Deformation features underneath the adjacent region of indentation, (f) Schematic of the slip planes in β-ODZ.

and $(2\bar{1}\bar{1}2)$ slip bands and produce a serial of steps at their intersections. For α-Ti, prismatic $\langle a \rangle$ slip is dominant at room temperature, while the basal and pyramidal $\langle a \rangle$ slip require much higher critical resolved shear stress (CRSS) [48,49]. However, no prismatic slip was observed in current oxygen-enriched α phase. With the increasing of oxygen concentration, the most favorable slip system in α-Ti has been altered, and the basal slip becomes the easiest one. Fig. 4(d) plots the geometrical relationship between the three activated slip planes, (0002), $(\bar{2}112)$ and $(2\bar{1}\bar{1}2)$.

Fig. 5(a) shows the SEM micrographs of an indentation in the β-ODZ, which is 350 μm away from the sample surface. High density of parallel slip bands is formed along both $(2\bar{1}1)$ and $(\bar{2}\bar{3}3)$ planes underneath the indentation, as shown in Fig. 5(b). The slip bands along $(2\bar{1}1)$ plane are much denser than those in $\alpha+\beta$ ODZ, indicating that the β-ODZ has strong capability to coordinate plastic deformation than that of the relative brittle α phase in the $\alpha+\beta$ ODZ. In addition, the slip bands along $(\bar{2}\bar{3}3)$ crystallographic planes display some bent features, as marked in Fig. 5(c). In the region far from the indentation, a few slip bands along the $(21\bar{1})$ planes were developed, as shown in Figs. 5(d) and (e). Some dislocations are observed in between those slip bands along $(21\bar{1})$. However, the $(\bar{2}\bar{3}3)$ plane is not a common slip plane in β phase, which interacts an angle of 25° respect to the $(01\bar{1})$ plane. This observation likely hints that the increasement of oxygen concentration changes the slip plane in β-Ti. Fig. 5(f) plots the geometrical relationship between the activated slip planes in the β-ODZ.

Fig. 6(a) shows the morphology of indentation that is 1350 μm away from surface at the β-NOZ. Shallow slip traces appear around the indentation, as marked by the white arrows. TEM foil was cut at the region marked by white dash line in Fig. 6(a). As a result of flexible plastic deformation, multiple glide systems were activated along $(12\bar{1})$, $(1\bar{2}1)$, $(3\bar{2}1)$ and $(32\bar{1})$ crystallographic planes, which are conventional a/2 $\langle 111 \rangle$ slip systems for BCC metals [50,51]. For the β-NOZ, slip bands along $(1\bar{2}1)$ and $(3\bar{2}1)$ planes in the central indentation are much thinner and denser than those in β-ODZ, as marked in Fig. 6(b). The slip bands are slightly misplaced as tiny shear steps produce at their intersections in Fig. 6(c). In the region far from the indentation, the spacing of slip bands increases compared with those in the shallow region underneath the indentation, as shown in Figs. 6(d) and (e). Fig. 6(f) plots the activated slip planes in the β-NOZ. The β-NOZ are easy to deform and play a key role of buffering during plastic deformation of the oxygen-charged β-Ti.

3.4. Compressive behavior of oxygen-charged β-Ti

Fig. 7 shows the compressional behavior of β-Ti alloy with and without oxygen-charging. According to the engineering stress-strain curve in Fig. 7, the yield strength of ORI-β-Ti is 727 MPa and the failure compressive strain is ~36%. With addition of oxygen gradient distribution, the yield strength of two samples increases to 914 MPa and 1065 MPa, respectively. The ultimate compressive strength of OC4h-β-Ti reaches 1.7 GPa because the oxygen gradient distribution enhances strain hardening [36–38]. Notably, both the oxygen-charged samples have even greater compressive strains compared with that of ORI-β-Ti (~39%). In particular, the oxygen-charged β-Ti alloys show an upturning trend in the stress-strain curve at the end of compression, indicating that the β-NOZ ductile core starts to function and avoids sample catastrophic failure. The insets of Fig. 7 are low-magnification images showing the compressed samples. All the failed samples have a nearly 45° shear crack in respect to the loading axis. The lateral surface of ORI-β-Ti only has one major crack and the remaining parts are almost smooth. However, both of the oxygen

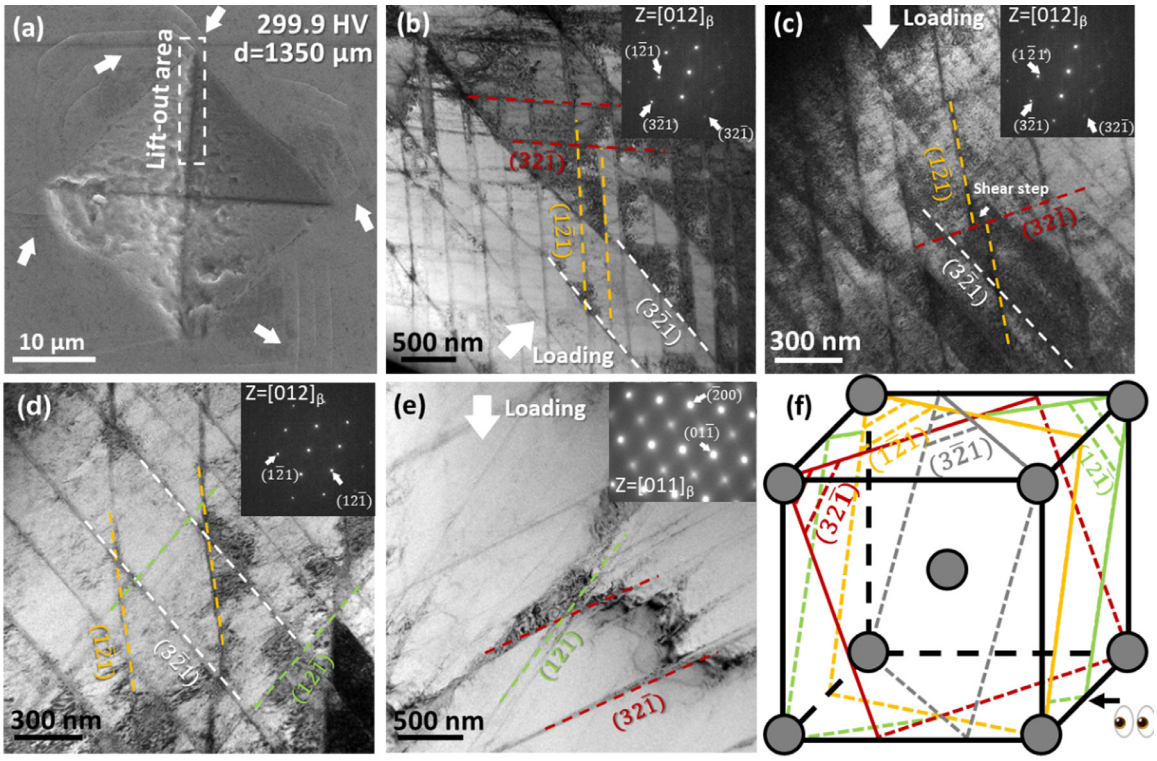

Fig. 6. Deformation mechanism in β-NOZ. (a) SEM micrograph of an indentation in β-NOZ. (b) TEM micrographs showing the characteristics of slip bands under indentation. (c) Slip lines in shallow region underneath the indentation. (d) Slip lines in deep region underneath the indentation. (e) Deformation features in the region adjacent to the indentation. (f) Schematic of the slip planes in β-NOZ.

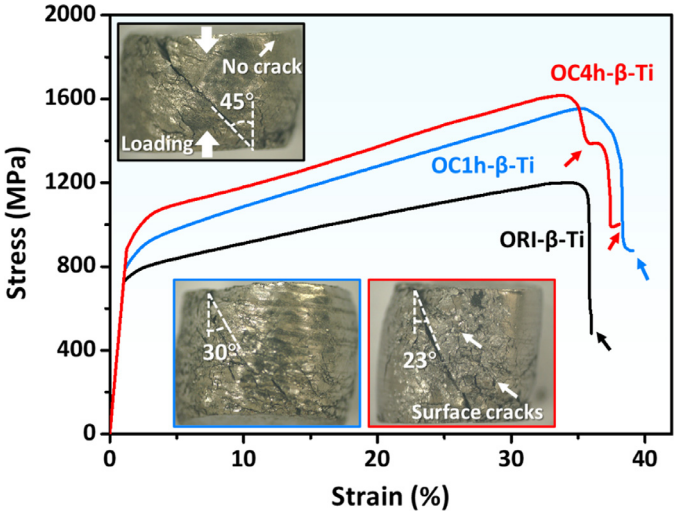

Fig. 7. Compressive stress-strain curve of ORI-β-Ti and OC-β-Ti (1 h and 4 h). The insets showing the deformation features on the surface of the failed samples after compression. Both OC-β-Ti samples display an upturn in the stress-strain curve at the end of compression.

charged β-Ti alloys have multiple cracks on the outer surface in addition to the major crack. Furthermore, the major crack in the OC-β-Ti deviates from the classical 45° shear (30° for OC1h-β-Ti and 23° for OC4h-β-Ti), which is a typical feature for high strength materials [52]. All of these observations indicate that the oxygen-charging induced oxygen gradient distribution makes β-Ti alloys much tougher and stronger than the ORI-β-Ti. Oxygen solute gradient distribution and phase variations endow OC-β-Ti with the capacity to bear more plastic deformation or even surface crack damage, which is a merit of oxygen-charged β-Ti alloy.

All the ORI-β-Ti, OC1h-β-Ti and OC4h-β-Ti samples display transgranular quasi-cleavage fracture morphologies. Fracture surface of ORI-β-Ti is comparatively smooth, as shown in Figs. 8(a) to (b). Typical cleavage steps are observed on the fracture surface of oxygen-charged sample in Figs. 8(d) and (g). The lateral surface after fracture is distinctive due to the effect of oxygen solute gradient and phase variation. Hardly any crack is visible as a result of homogenous deformation of ORI-β-Ti, as shown in Fig. 8. In contrast to fracture pattern of ORI-β-Ti, profuse slip traces and massive cracks develop in the surface of OC1h-β-Ti, as marked by arrows in Figs. 8(e) and (f). The localized slip traces are seen as cradle of nucleation of cracks which further evolve into tiny cracks, then subsequently expand with increasing of compressive force, but cannot propagate across the whole sample. The OC4h-β-Ti sample embodies a distinctive feature that the top surface after fracture is similar to a deformed rock, as shown in Fig. 8(h). Some blocks of the top layer in OC4h-β-Ti were drop (Fig. 8(h). Vast tiny cracks and large cracks spread all over top layer of oxygen-charged samples as shown in Fig. 8(k). The formation of numerous surface cracks but not propagating further is a way to absorb deformation energy and a major tough mechanism in the oxygen-charged β-Ti.

3.5. Abrasive behavior of oxygen-charged β-Ti

Fig. 9 shows the influence of solute oxygen gradient on the abrasive behavior of oxygen-charged β-Ti. The OC4h-β-Ti has much lower material removal under wear test, as shown in Fig. 9(a). Its weight loss is 30% lessen and the wear rate is reduced to one third of the ORI-β-Ti. The surface roughness is decreased by 40% compared with that of ORI-β-Ti, which confirms that the

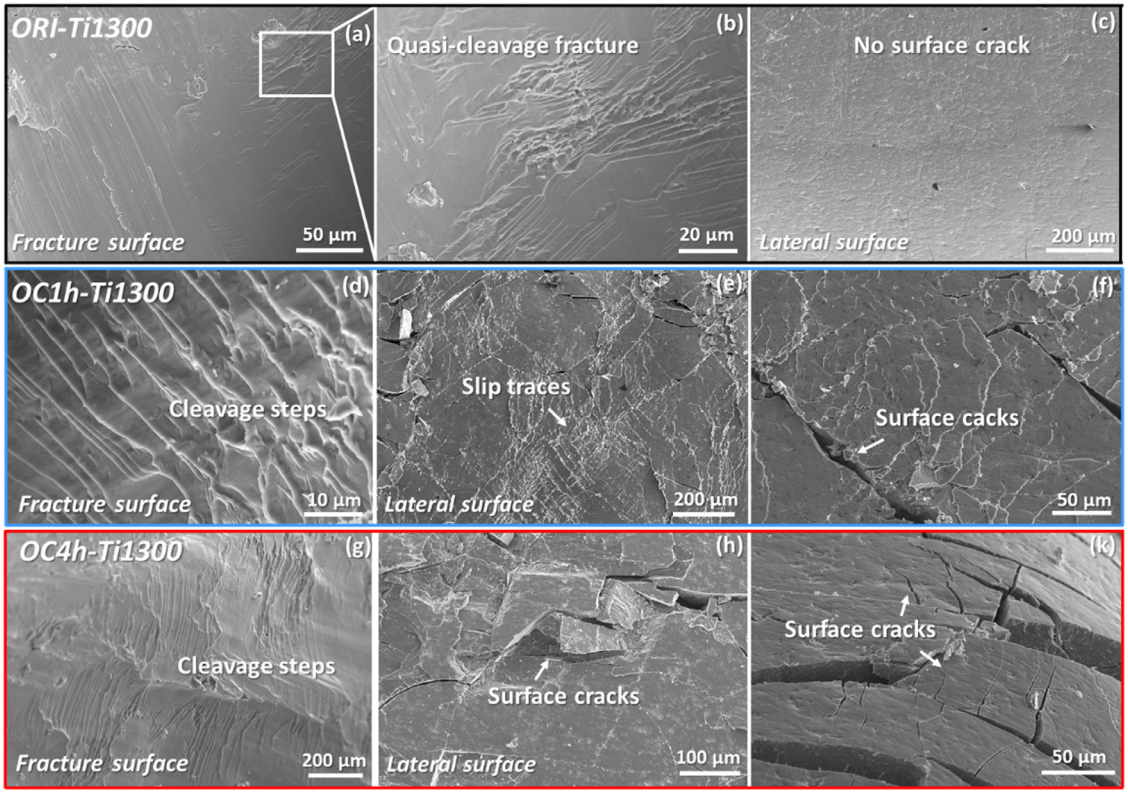

Fig. 8. SEM images of fracture surface and lateral surface of ORI-β-Ti, OC1h-β-Ti and OC4h-β-Ti after compression. (a) to (c) Fracture features in ORI-β-Ti, (d) to (f) Fracture features in OC1h-β-Ti. (g) to (k) Fracture features in OC4h-β-Ti.

oxygen-charging treatment has remarkably improved abrasive resistance of β-Ti. The 3D laser morphology after the abrasion test has been analyzed and shown in Figs. 9(c) and (d). The worn surfaces exhibit typical parallel plowing features, which are attributed to the difference of surface hardness between the tested samples and the SiC abrasive. During the abrasive test, surface of ORI-β-Ti samples was penetrated and removed by the harder SiC behaving as tested surface was scraped off. After oxygen-charging process, the depth of delamination wear becomes much lower and the plowing groove width changes to narrower ones, as shown in Fig. 9(c). Besides, the level of furrow delamination is reduced. The variation in worn morphology is mutually authenticated with data of abrasion test. The synergy of oxygen gradient distribution and the superhard α phase coating around β matrix is the main reason for the promoted abrasive resistance of oxygen-charged β-Ti.

4. Discussion

The synergy effects of oxygen gradient and heterogeneous phase variations make β-Ti alloy with ultrahigh hardness, strength, toughness, and enhanced wear-resistance. Next, we briefly discuss the effect of oxygen gradient on remarkable mechanical performance of β-Ti alloy.

4.1. Origin of ultrahigh hardening and wear-resistance

Due to the diffusion of oxygen atoms, oxygen-charged β-Ti has an oxygen-gradient distribution from the sample surface to the interior. Once the concentration of oxygen reaches a critical value, a layer of α phase is formed since oxygen solutes promote β to α phase transformation [53]. As a result of combined effects of superhigh oxygen level and ultra-hard α-lath, the hardness of oxygen-charged sample reaches an ultrahigh value of 1125 HV (Fig. 3). The ultrahigh hardness is owing to two effects: oxygen solute hardening and precipitation of oxygen enriched α-Ti. Solid solution strengthening generally accounts for the interaction between solute atoms and dislocations, which originates from the local lattice distortion caused by the solutes [54]. Besides, oxygen-vacancy complexes trap screw dislocations, triggering ultrahigh hardening and strengthening as well [36–38]. The maximum solubility of oxygen in HCP α-Ti is about 14.5 wt.%, which is much higher than that in BCC β phase (about 2 wt.% at 1273 K) [24]. Thus, enrich of oxygen induces extremely high strengthening in HCP α phase. Besides, the size of α lath is fined, which also contributes to the hardening due to the Hall-Petch strengthening [55]. Such combination of gradient microstructures, i.e. superhard α phases wrapped around β matrix with oxygen-gradient strengthening endows this β-Ti alloy with marvelous capacity to resist plastic deformation and abrasive wear, as displayed in Fig. 9.

4.2. Strengthening and damage resistance of oxygen gradient β-Ti alloy

The solution of oxygen atoms remarkably improves compressive strength, while no sacrifice in total compressive strains thanks to the excellent adhesion between the heterogeneous $\alpha+\beta$ ODZ layer with the β-matrix. The oxygen-charging induced gradient phase and oxygen distribution endow β-Ti with marvelous toughness and outstanding ability to resist crack damage than the ORI-β-Ti. Albeit profuse slip traces forming on lateral surface in Fig. 8(e), strain localization in $\alpha+\beta$ ODZ does not induce premature failure of OC-β-Ti. On the contrary, compressive strain of OC-β-Ti is even better (Fig. 7) than that of ORI-β-Ti due to the partition of plastic deformation between the ductile β-Ti core and a hard $\alpha+\beta$ ODZ layer. The softer core of β-NOZ bears most of the applied strain and the harder shell of $\alpha+\beta$ ODZ layer resist most of the applied

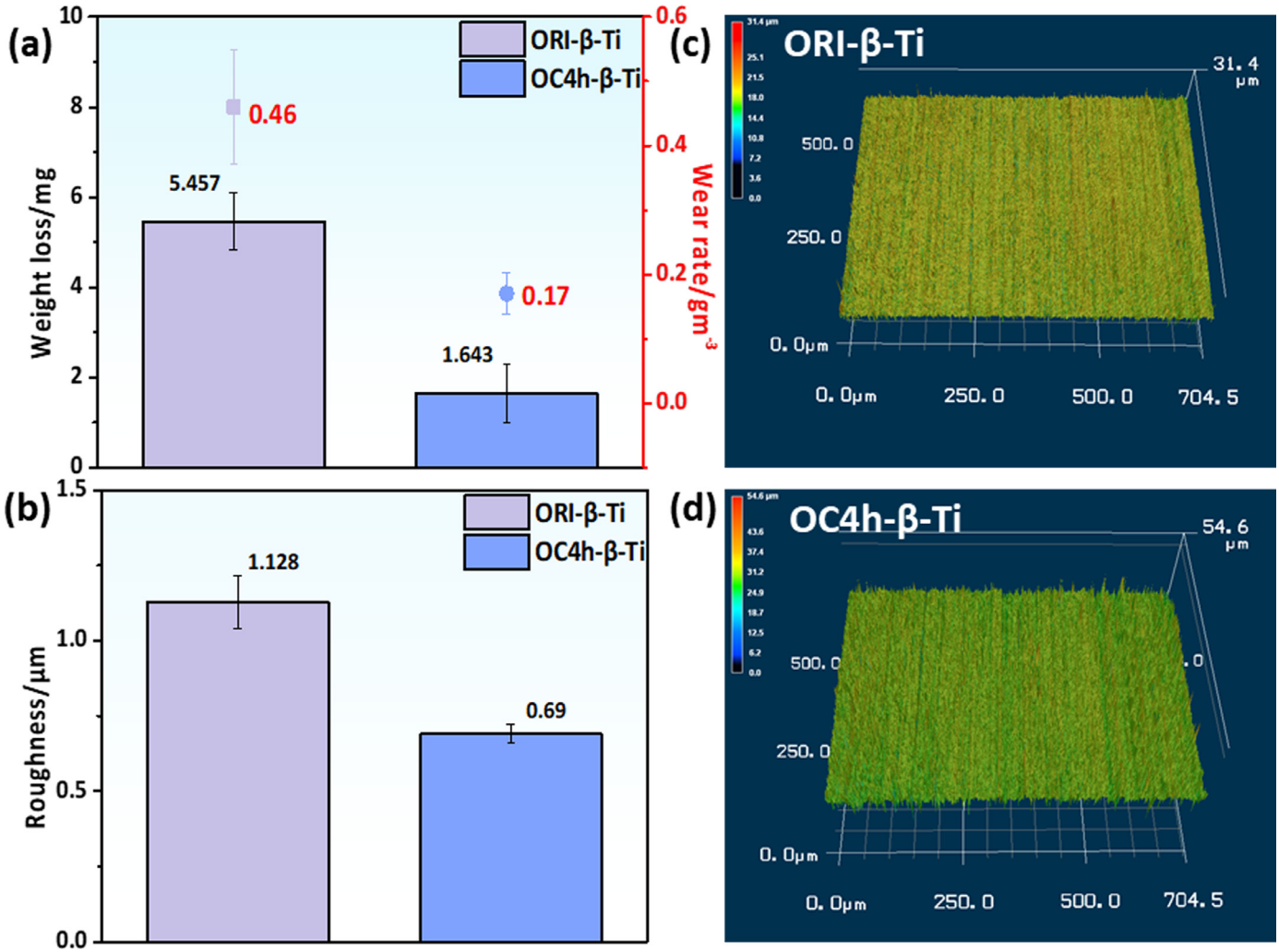

Fig. 9. Two-body abrasive wear behavior of ORI-β-Ti and OC4h-β-Ti. (a) Weight loss and wear rate. (b) Surface roughness. 3D laser morphologies of the attrition tested (c) ORI-β-Ti and (d) OC4h-β-Ti were subjected to SiC abrasive at the normal load of 3 N.

load. The β-ODZ region has a certain capability to offset part of localized strain concentration. With the proceeding of compression, high degree of shear stress localizes on some slip planes in the harder but brittle $\alpha+\beta$ ODZ so that cracks nucleate and spread around (Figs. 8(f), (h) and (k)), but these surface cracks cannot penetrate into the sample interior because of the oxygen gradient distribution region, which impedes and blunts the cracks. Thus, the ductility of OC-β-Ti is not adversely affected by the ultrahardening exterior although formation of profuse surface cracks (Fig. 8(d)).

4.3. Perspective of oxygen-charging in Ti-based biomedical implants

The mechanical behavior of oxygen-charged β-Ti is compared with other commonly used biomedical Ti alloys with conventional surface modification. The yield strength (Fig. 10(a)), maximum strength (Fig. 10(b) versus ductility and hardness versus layer thickness of modified Ti (Fig. 10(c)) are plotted. The dashed curves in Figs. 10(a) and (b) mark the border of tensile and compressive properties of some biomedical Ti alloys respectively. It is clear that the oxygen-charged β-Ti stands out [4,56-61], displaying combination of ultrahigh strength, deformability and high strain hardening. For biomedical implants, compressive data is more reliable and useful because implants such as joints and teeth usually bear compressive stress in human daily life. In addition to ultrahigh strength and ductility, the oxygen-charged β-Ti also has ultrahigh hardness and thick impact zone [18,45-47,62-64], as shown in Fig. 10(c). Thus, service life of oxygen-charged biomedical Ti alloys is likely longer. Conventional treatments including oxide coating, nitriding, ion implantation etc. are quite difficult to achieve the combination of superior mechanical properties and wear resistance together. The advantages of current oxygen-charging technique are summarized as below. First, interfacial separation may hardly happen under repeated loading condition because of indivisibility caused by the oxygen-gradient distribution. Second, the depth of ultrahard α phase coating (~200 μm) plus oxygen gradient region (~600 μm) is much thicker than those of nitriding or thermal oxide. Third, oxygen-charged Ti alloys achieve anomalous synergy of high strength and toughness and the ability to resist catastrophic failure. By controlling the time of oxygen-charging, one can easily regulate oxygen level and the diffusing distance of oxygen atom in the bulk sample to manipulate the mechanical performance of implants. Lastly, oxygen-charging process is suitable for large-scale production and a wide range of metallic materials. It is suitable for BCC metallic materials (such as Nb, Ta and V etc.), and also can be used to process metallic materials with high temperature BCC phase, such as pure Ti and Zr etc. Therefore, the oxygen-charging strategy possesses a far-reaching outlook for development of high-performance Ti biomedical implants which are more durable, reliable and economical.

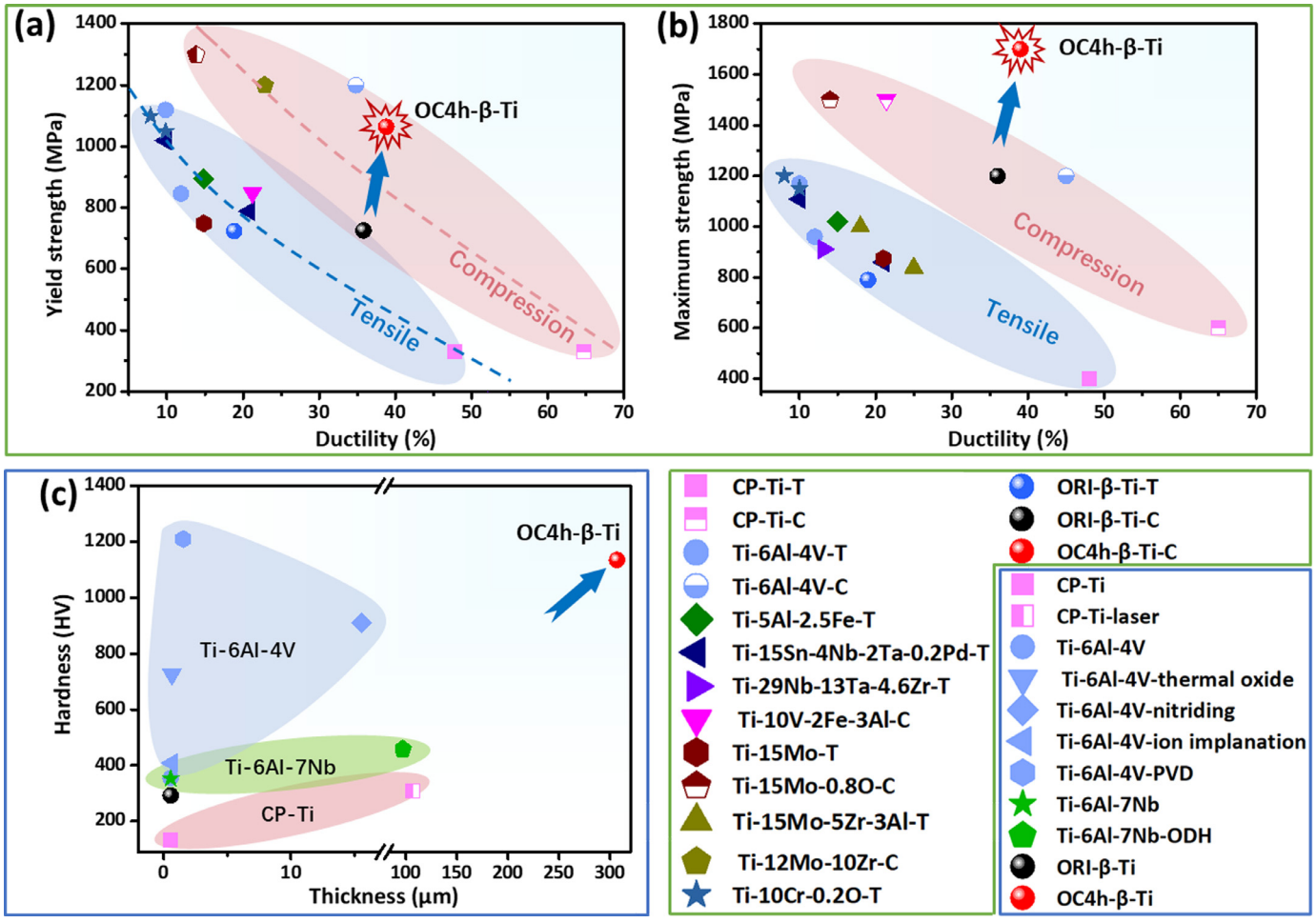

Fig. 10. Comparison of the mechanical properties of OC4h-β-Ti with other biomedical Ti alloys [4,56-61]. (a) Yield strength vs. Ductility and (b) Maximum strength vs. Ductility. (c) Hardness versus hardened layer thickness plot for OC4h-β-Ti, ORI-β-Ti and other biomedical Ti alloys with conventional surface modification [18,45-47,62-64]. T is short for tension and C is short for compression.

5. Conclusion

In this study, a promising β-Ti alloy with combined gradient phase structures and oxygen distribution is fabricated. Oxygen solutes strengthen β-Ti alloy through the formation of ultra-hard α laths layer and an oxygen gradient distribution region, which leads to a synergy of ultrahigh hardness, strength and wear-resistance. Deformation mechanisms controlled by oxygen solutes transform from simple but unusual basal slip in α phase to multiple-slip activities in β phase. Through the formation of numerous surface cracks under loading, OC-β-Ti achieves high toughness and has the ability to resist catastrophic failure owing to a ductile oxygen-free core. The excellent mechanical properties of oxygen-charged β-Ti pave the way for the development of reliable, durable and economic biomedical implants.

Declaration of Competing Interest

The metal oxygen-charging technology has been submitted for patenting.

Acknowledgements

This research was supported by National Natural Science Foundation of China (Grant Nos. 51922082 and 51971170) and the 111 Project of China (Grant Number BP2018008). X.Q.W would like to thank Mr. Qiang Li for abrasion tests and Mr. Jian Zhang for sample preparation.

References

[1] J.D. Cotton, R.D. Briggs, R.R. Boyer, S. Tamirisakandala, P. Russo, N. Shchetnikov, J.C. Fanning, State of the art in beta titanium alloys for airframe applications, JOM 67 (6) (2015) 1281–1303.
[2] R.R. Boyer, Titanium for aerospace: rationale and applications, Adv. Perform. Mater. 2 (4) (1995) 349–368.
[3] K. Wang, The use of titanium for medical applications in the USA, Mat. Sci. Eng. A 213 (1–2) (1996) 134–137.
[4] M. Geetha, A.K. Singh, R. Asokamani, A.K. Gogia, Ti based biomaterials, the ultimate choice for orthopaedic implants – a review, Prog. Mater. Sci. 54 (3) (2009) 397–425.
[5] M. Long, H.J. Rack, Titanium alloys in total joint replacement–a materials science perspective, Biomaterials 19 (18) (1998) 1621–1639.
[6] R.R. Boyer, Attributes, characteristics, and applications of titanium and its alloys, JOM 62 (5) (2010) 21–24.
[7] C. Leyens, M. Peters, Titanium and Titanium Alloys Fundamentals and Applications, Wiley-VCH Verlag GmbH & Co. KGaA, Weinheim, 2003.
[8] M. Niinomi, Mechanical properties of biomedical titanium alloys, Mat. Sci. Eng. A 243 (1–2) (1998) 231–236.
[9] G. Lütjering, J.C. Williams, Titanium, 2nd ed., Springer, Berlin, 2007.
[10] N.J. Hallab, J.J. Jacobs, Orthopedic implant fretting corrosion, Corros. Rev. 21 (2–3) (2003) 183–213.
[11] K.G. Budinski, Tribological properties of titanium alloys, Wear 151 (2) (1991) 203–217.
[12] S.S. Perry, J.W. Ager, G.A. Somorjai, R.J. McClelland, M.D. Drory, Interface characterization of chemically vapor deposited diamond on titanium and Ti-6Al-4V, J. Appl. Phys. 74 (12) (1993) 7542–7550.
[13] A. Loinaz, M. Rinner, F. Alonso, J.I. Onate, W. Ensinger, Effects of plasma immersion ion implantation of oxygen on mechanical properties and microstructure of Ti6Al4V, Surf. Coat. Technol. 104 (1998) 262–267.

[14] M. Aliofkhazraei, R.S. Gharabagh, M. Teimouri, M. Ahmadzadeh, G.B. Darband, H. Hasannejad, Ceria embedded nanocomposite coating fabricated by plasma electrolytic oxidation on titanium, J. Alloys Compd. 685 (2016) 376–383.
[15] S. Fayeulle, Tribological behavior of nitrogen-implanted materials, Wear 107 (1) (1986) 61–70.
[16] B. Größner-Schreiber, J. Teichmann, M. Hannig, C. Dörfer, D.F. Wenderoth, S.J. Ott, Modified implant surfaces show different biofilm compositions under in vivo conditions, Clin. Oral Implant Res. 20 (2009) 817–826.
[17] D. Dunn, S. Raghavan, Formation and characterization of anodized layers on Cp Ti and Ti-6Al-4V biomaterials, Surf. Coat. Technol. 50 (3) (1992) 223–232.
[18] R.M. Streicher, H. Weber, R. Schön, M. Semlitsch, New surface modification for Ti-6Al-7Nb alloy: oxygen diffusion hardening (ODH), Biomaterials 12 (2) (1991) 125–129.
[19] A. Bloyce, P.Y. Qi, H. Dong, T. Bell, Surface modification of titanium alloys for combined improvements in corrosion and wear resistance, Surf. Coat. Technol. 107 (2–3) (1998) 125–132.
[20] R. Sonntag, J. Reinders, J.P. Kretzer, What's next? Alternative materials for articulation in total joint replacement, Acta Biomater. 8 (7) (2012) 2434–2441.
[21] K. Chou, E.A. Marquis, Oxygen effects on ω and α phase transformations in a metastable β Ti–Nb alloy, Acta Mater. 181 (2019) 367–376.
[22] H. Conrad, Diffusion rates in inorganic nuclear materials, Prog. Mater. Sci. (1981).
[23] H. Conrad, Effect of interstitial solutes on the strength and ductility of titanium, Prog. Mater. Sci. 26 (1981) 138.
[24] T.B. Massalski, H. Okamoto, P.R. Subramanian, L. Kacprzak, Binary Alloy Phase Diagrams, 2nd ed., ASM International, 1990.
[25] Z. Liu, G. Welsch, Effects of oxygen and heat-treatment on the mechanical-properties of alpha and beta titanium-alloys, Metall. Trans. A 19 (3) (1988) 527–542.
[26] R.O. Ritchie, The conflicts between strength and toughness, Nat. Mater. 10 (2011) 817–822.
[27] X. Li, L. Lu, J. Li, X. Zhang, H. Gao, Mechanical properties and deformation mechanisms of gradient nanostructured metals and alloys, Nat. Rev. Mater. 5 (9) (2020) 706–723.
[28] Z. Liu, M.A. Meyers, Z. Zhang, R.O. Ritchie, Functional gradients and heterogeneities in biological materials: design principles, functions, and bioinspired applications, Prog. Mater. Sci. 88 (2017) 467–498.
[29] S. Suresh, Graded materials for resistance to contact deformation and damage, Science 292 (2001) 2447–2451.
[30] X.H. An, Structural hierarchy defeats alloy cracking, Science 373 (6557) (2021) 857–858.
[31] Z. Cheng, H. Zhou, Q. Lu, H. Gao, L. Lu, Extra strengthening and work hardening in gradient nanotwinned metals, Science 362 (2018) eaau1925.
[32] J.W. Zhang, I.J. Beyerlein, W.Z. Han, Hierarchical 3D nanolayered duplex-phase Zr with high strength, strain Hardening, and ductility, Phys. Rev. Lett. 122 (25) (2019) 255501.
[33] L.L. Li, Y. Su, I.J. Beyerlein, W.Z. Han, Achieving room-temperature brittle–to-ductile transition in ultrafine layered Fe-Al alloys, Sci. Adv. 6 (39) (2020) eabb6658.
[34] G. Michal, F. Ernst, H. Kahn, Y. Cao, F. Oba, N. Agarwal, A. Heuer, Carbon supersaturation due to paraequilibrium carburization: stainless steels with greatly improved mechanical properties, Acta Mater. 54 (6) (2006) 1597–1606.
[35] Q. Yu, L. Qi, T. Tsuru, R. Traylor, D. Rugg, J.W. Morris Jr., M. Asta, D.C. Chrzan, A.M. Minor, Origin of dramatic oxygen solute strengthening effect in titanium, Science 347 (6222) (2015) 635–639.
[36] P.J. Yang, Q.J. Li, W.Z. Han, J. Li, E. Ma, Designing solid solution hardening to retain uniform ductility while quadrupling yield strength, Acta Mater. 179 (2019) 107–118.
[37] P.J. Yang, Q.J. Li, T. Tsuru, S. Ogata, J.W. Zhang, H.W. Sheng, Z.W. Shan, G. Sha, W.Z. Han, J. Li, E. Ma, Mechanism of hardening and damage initiation in oxygen embrittlement of body-centred-cubic niobium, Acta Mater. 168 (2019) 331–342.
[38] J. Zhang, W.Z. Han, Oxygen solutes induced anomalous hardening, toughening and embrittlement in body-centered cubic vanadium, Acta Mater. 196 (2020) 122–133.
[39] P.J. Yang, W.Z. Han, Enhanced oxidation resistance in refractory niobium by surface Ti+/Si+ implantation, Corros. Sci. 163 (2020) 108297.
[40] M. Song, S. Han, D. Min, G. Choi, J. Park, Diffusion of oxygen in β-titanium, Scr. Mater. 59 (6) (2008) 623–626.
[41] N. Birks, G.H. Meier, F.S. Pettit, Introduction to the High-Temperature Oxidation of Metals, 2nd ed., Cambridge Univ Pr, Cambridge, 2006.
[42] R. Kolli, A. Devaraj, A review of metastable beta titanium alloys, Metals 8 (7) (2018).
[43] T. Furuhara, S. Takagi, H. Watanabe, T. Maki, Crystallography of grain boundary α precipitates in α β titanium alloy, Metall. Trans. A 27 (1996) 1635–1646.
[44] W.G. Burgers, On the process of transition of the cubic-body-centered modification into the hexagonal-close-packed modification of zirconium, Physica D 1 (1934) 561–586.
[45] H. Wu, L. Xie, M. He, R. Zhang, Y. Tian, S. Liu, T. Gong, F. Huo, T. Yang, Q. Zhang, S. Guo, W. Tian, A wear-resistant TiO2 nanoceramic coating on titanium implants for visible-light photocatalytic removal of organic residues, Acta Biomater. 97 (2019) 597–607.
[46] H. Guleryuz, H. Cimenoglu, Effect of thermal oxidation on corrosion and corrosion-wear behaviour of a Ti-6Al-4V alloy, Biomaterials 25 (16) (2004) 3325–3333.
[47] J.A. García, R. Martínez, B. Lerga, G.G. Fuentes, R.J. Rodríguez, S. Mändl, Tribological improvements of ion implanted technological alloys: plasma immersion vs. conventional ion implantation, Surf. Coat. Technol. 200 (1–4) (2005) 573–578.
[48] A.T. Churchman, The slip modes of titanium and the effect of purity on their occurrence during tensile deformation of single crystals, Proc. R. Soc. Lond. Ser. A 226 (1165) (1954) 216–226.
[49] J. Gong, A.J. Wilkinson, Anisotropy in the plastic flow properties of single-crystal α titanium determined from micro-cantilever beams, Acta Mater. 57 (19) (2009) 5693–5705.
[50] P. Castany, M. Besse, T. Gloriant, In situ TEM study of dislocation slip in a metastable β titanium alloy, Scr. Mater. 66 (6) (2012) 371–373.
[51] M. Besse, P. Castany, T. Gloriant, Mechanisms of deformation in gum metal TNTZ-O and TNTZ titanium alloys: a comparative study on the oxygen influence, Acta Mater. 59 (15) (2011) 5982–5988.
[52] Z.F. Zhang, G. He, J. Eckert, L. Schultz, Fracture mechanisms in bulk metallic glassy materials, Phys. Rev. Lett. 91 (4) (2003) 045505.
[53] Z. Liu, G. Welsch, Literature survey on diffusivities of oxygen, aluminum, and vanadium in alpha-titanium, beta-titanium, and in rutile, Metall. Trans. A 19 (4) (1988) 1121–1124.
[54] B. Sun, S. Li, H. Imai, T. Mimoto, J. Umeda, K. Kondoh, Fabrication of high--strength Ti materials by in-process solid solution strengthening of oxygen via P/M methods, Mater. Sci. Eng. A 563 (2013) 95–100.
[55] N. Hansen, Hall-Petch relation and boundary strengthening, Scr. Mater. 51 (2004) 801–806.
[56] M. Niinomi, Mechanical properties of biomedical titanium alloys, Mat. Sci. Eng. A 243 (1–2) (1998) 231–236.
[57] F. Geng, M. Niinomi, M. Nakai, Observation of yielding and strain hardening in a titanium alloy having high oxygen content, Mat. Sci. Eng. A 528 (16–17) (2011) 5435–5445.
[58] H. Liu, M. Niinomi, M. Nakai, K. Cho, K. Narita, M. Sen, H. Shiku, T. Matsue, Mechanical properties and cytocompatibility of oxygen-modified beta-type Ti-Cr alloys for spinal fixation devices, Acta Biomater. 12 (2015) 352–361.
[59] J. Suryawanshi, G. Singh, S. Msolli, M.H. Jhon, U. Ramamurty, Tension-compression asymmetry and shear strength of titanium alloys, Acta Mater. (2021) 117392.
[60] X. Ma, Z. Chen, L. Xiao, W. Lu, S. Luo, Y. Mi, Compressive deformation of a metastable β titanium alloy undergoing a stress-induced martensitic transformation: the role of β grain size, Mater. Sci. Eng. A 794 (2020) 139919.
[61] J. Zhang, B. Qian, Y. Wu, Y. Wang, J. Cheng, Z. Chen, J. Li, F. Sun, F. Prima, A kink-bands reinforced titanium alloy showing 1.3GPa compressive yield strength: towards extra high-strength/strain-transformable Ti alloys, J. Mater. Sci. Technol. 74 (2021) 21–26.
[62] L.C. Zhang, L.Y. Chen, A review on biomedical titanium alloys: recent progress and prospect, Adv. Eng. Mater. 21 (4) (2019).
[63] M. Łępicka, M. Grądzka-Dahlke, D. Pieniak, K. Pasierbiewicz, K. Kryńska, A. Niewczas, Tribological performance of titanium nitride coatings: a comparative study on TiN-coated stainless steel and titanium alloy, Wear 422-423 (2019) 68–80.
[64] A.F. Yetim, A. Alsaran, I. Efeoglu, A. Çelik, A comparative study: the effect of surface treatments on the tribological properties of Ti–6Al–4V alloy, Surf. Coat. Technol. 202 (11) (2008) 2428–2432.